A two-scale Weibull approach to the failure of porous ceramic structures made by robocasting: possibilities and limits

Martin Genet, Manuel Houmard, Salvador Eslava, Eduardo Saiz, Antoni P. Tomsia

A two-scale Weibull approach to the failure of porous ceramic structures made by robocasting: possibilities and limits

Martin Genet[a,1,*], Manuel Houmard[a,2], Salvador Eslava[b], Eduardo Saiz[b], Antoni P. Tomsia[a]

[a] *Materials Science Division, Lawrence Berkeley National Laboratory, California, USA*
[b] *Centre for Advanced Structural Ceramics, Department of Materials, Imperial College London, UK*

Abstract

This paper introduces our approach to modeling the mechanical behavior of cellular ceramics, through the example of calcium phosphate scaffolds made by robocasting for bone-tissue engineering. The Weibull theory is used to deal with the scaffolds' constitutive rods statistical failure, and the Sanchez-Palencia theory of periodic homogenization is used to link the rod- and scaffold-scales. Uniaxial compression of scaffolds and three-point bending of rods were performed to calibrate and validate the model. If calibration based on rod-scale data leads to over-conservative predictions of scaffold's properties (as rods' successive failures are not taken into account), we show that, for a given rod diameter, calibration based on scaffold-scale data leads to very satisfactory predictions for a wide range of rod spacing, i.e. of scaffold porosity, as well as for different loading conditions. This work establishes the proposed model as a reliable tool for understanding and optimizing cellular ceramics' mechanical properties.

Keywords:
Cellular ceramics ; Fracture ; Mechanical properties ; Strength ;

*Corresponding author. Mail address: Lawrence Berkeley National Laboratory, One Cyclotron Road MS62-0237, Berkeley, CA-94720, USA. Tel: 1-510-486-6809. E-mail address: mgenet@lbl.gov.

[1] Current affiliation: Marie-Curie Fellow, Cardiac Biomechanics Laboratory, Department of Surgery, University of California at San Francisco, USA.

[2] Current affiliation: Assistant Professor, Department of Metallurgical and Materials Engineering, School of Engineering, Federal University of Minas Gerais, Belo Horizonte, Brazil.

Contents

1. Introduction

Robocasting, also called direct-write assembly or solid freeform fabrication, is considered one of the top candidates for processing highly complex materials [Smay et al., 2002; Leong et al., 2003]. It consists of building three-dimensional structures, or scaffolds, layer-by-layer by extruding a continuous filament, or rod, through a tip guided by a computer-assisted positioning system [Saiz et al., 2007; Russias et al., 2007; Houmard et al., 2012b]. It allows very precise control of the scaffold's macroscopic porosity, and allows the processing of a large range of materials, including bio-ceramics [Miranda et al., 2006] and bio-glass [Fu et al., 2011]. It is useful in many different areas, including battery electrodes [Liu et al., 2011], photonic crystals [Gratson et al., 2006], and tissue engineering [Woodard

et al., 2007; Lan Levengood et al., 2010].

Mechanical properties and reliability are key parameters in the application of any scaffold. For example, in bone-tissue engineering, stiffness plays a major role in cell proliferation toward bone growth [Woodard et al., 2007; Miranda et al., 2008b], while strength determines the capability to withstand *in vivo* loading [Woodard et al., 2007; Miranda et al., 2008b]. Thus, it is necessary to quantitatively understand the scaffold's mechanics (including elastic behavior, damage mechanisms, *etc.*), and to derive reliable structure-properties relations. This effort requires the development of theoretical models and associated prediction tools along with experimental analysis. Such models, once carefully validated, will reduce the need for extremely time- and resource-consuming experiments, and will allow prediction of any scaffold's behavior at no cost.

Several analysis have been proposed in the literature to improve the understanding of the mechanics of robocast scaffolds, but a general computational framework with strong mechanical basis is still missing. For instance, the Finite Element (FE) method has been used to compute the elastic response of assemblies of rods and to elucidate the possible failure modes in compression and shear [Miranda et al., 2008a], but the analysis was based upon a critical stress criterion, which can be extremely mesh-dependent, and did not deal with the statistical aspect of failure. The classical Weibull framework has been used to deal with scaffold failure [Miranda et al., 2008b; Yang et al., 2010], but as the analysis was solely driven at the scaffold scale, it did not allow for an extrapolation of the role of the scaffold architecture outside the experimental domain. In another FE-based work, the effective properties of an element of volume representative of the scaffold's architecture were computed in order to analyze the influence of bone growth within the scaffold on stiffness [McIntosh et al., 2009], but strength was not studied.

In this paper, we propose a two-scale model of the mechanical behavior of scaffolds made by robocasting, that is intended to overcome the limitations of existing approaches. The proposed framework involves representations at both the rod, or *micro*, scale (100 μm) and scaffold, or *macro*, scale (10 mm), allowing to derive mechanically sound structure-properties relations. It is based on the Sanchez-Palencia theory of periodic homogenization [Sanchez-Palencia, 1974] and the Weibull theory of failure probability [Weibull, 1939, 1951]. Experimental rod and scaffold mechanical measurements are used in this paper for calibration and validation. We have focused on calcium phosphate (HA & HA/TCP) bio-scaffolds, but most of the conclusions should be

transferable to other compositions, and more generally to any quasi-brittle porous materials.

2. Materials & Methods

2.1. Uniaxial compression of scaffolds

Cubic scaffolds were processed following the method detailed in [Franco et al., 2010; Houmard et al., 2012a]. The scaffold structure used in this work consists of stacked layers of parallel rods forming 90° angles (see Figure 1). Four sets of scaffolds were printed for this paper, three made out of pure hydroxylapatite (HA), and one made out of a 60% hydroxylapatite / 40% tricalcium phosphate (HA/TCP) composite:

- In the first one (batch $S^{\mathrm{HA}}_{V=45\%}$), the rod spacing varied from 400 μm to 985 μm, and the rod diameter was adjusted from 200 μm to 610 μm, so that the porosity was kept constant at 45%.

- In the second and third ones (batches $S^{\mathrm{HA}}_{d=250\mu m}$ & $S^{\mathrm{HA}}_{d=200\mu m}$), the rod spacing varied from 350 μm to 870 μm (for batch $S^{\mathrm{HA}}_{d=250\mu m}$) or from 300 μm to 580 μm (for batch $S^{\mathrm{HA}}_{d=200\mu m}$), and the rod diameter was kept constant at 250 μm (for batch $S^{\mathrm{HA}}_{d=250\mu m}$) or 200 μm (for batch $S^{\mathrm{HA}}_{d=200\mu m}$), so that the porosity varied from 25% to 65% (for batch $S^{\mathrm{HA}}_{d=250\mu m}$) or from 35% to 65% (for batch $S^{\mathrm{HA}}_{d=200\mu m}$).

- The last one (batch $S^{\mathrm{HA/TCP}}_{d=250\mu m}$) is very similar to batch $S^{\mathrm{HA}}_{d=250\mu m}$, the only difference being that it is made out of HA/TCP instead of pure HA.

Previous dimensions refer to deposition conditions, sintering (1275°C for HA scaffolds; 1100°C for HA/TCP scaffolds; see [Houmard et al., 2012a] for further details) inducing a shrinkage of *ca.* 16% (for HA scaffolds) or *ca.* 8% (for HA/TCP scaffolds) [Houmard et al., 2012a].

For each set of microstructural parameters, between 3 and 8 scaffolds were printed and analyzed.

The scaffolds' mass and dimensions were measured after sintering, and their total porosity were deduced using the theoretical densities of HA (3.16 g/cm^3) and TCP (3.14 g/cm^3) [Houmard et al., 2012a]. And for each set of scaffolds with similar microstructure, the standard deviation for porosity is *ca.* 2%.

Uniaxial compression tests were performed on the processed scaffolds, using a servo-hydraulic testing machine (MTS810, MTS Systems, Eden

Prairie, MN, USA) with a cross-head speed of 0.2 mm/min (time-to-fracture *ca.* 30 s). These data have already been detailed in [Houmard et al., 2012a]. For batches $S^{\mathrm{HA}}_{V=45\%}$, $S^{\mathrm{HA}}_{d=250\mu m}$ & $S^{\mathrm{HA}}_{d=200\mu m}$, only the vertical (out-of-plane) direction was tested. For batch $S^{\mathrm{HA/TCP}}_{d=250\mu m}$, both the vertical and horizontal (in-plane) directions were tested.

The scaffolds' compressive strength were identified on the obtained force-displacement curves, as the maximum reached stress.

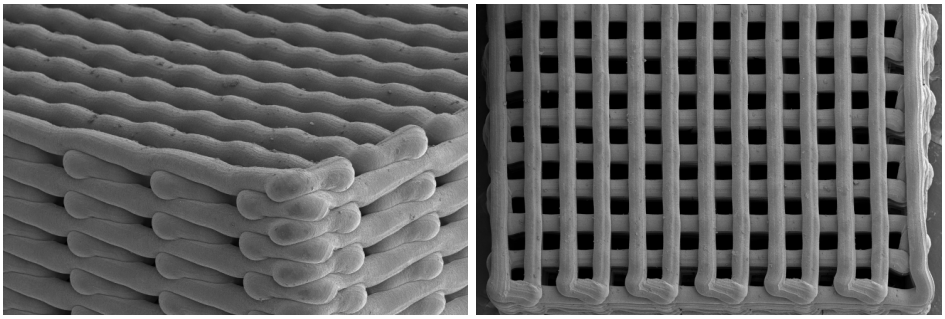

(a) Tilted view (b) Top view

Figure 1: Representative SEM images of scaffolds made by robocasting. The scaffolds are approximately 5 mm-side cubes.

2.2. Three-point bending of single rods

Single rods, *i.e.* the elementary constituents of robocast scaffolds, were processed by printing a single layer of lines. Because of strong adhesion with the substrate, some lines broke into several pieces during sintering. However, most of the pieces were long enough to be tested mechanically. Three sets of lines were printed: batches $R_{d=250\mu m}$, $R_{d=510\mu m}$ & $R_{d=840\mu m}$, respectively representing rods printed with a 250 μm-, 510 μm- & 840 μm-diameter tip, and respectively containing 16, 17 & 16 rods. After sintering (same sintering conditions than for the scaffolds), their diameter was 220 ± 30 μm, 390 ± 40 μm & 670 ± 60 μm, respectively. The rod diameters were chosen so as to cover the largest range possible of available tips, thus allowing to interpolate the rod data for any intermediate radius.

Three-point bending tests with a horizontal microindenter (Micro Materials) were performed on the rods to measure their flexural strength. Rods of 220 ± 30 μm-, 390 ± 40 μm- & 670 ± 60 μm-diameter were mounted on an aluminum holder atop 0.56 mm, 1.13 mm, & 1.76 mm trenches, respectively. They were bent by indenting at a constant load rate of 200 mN/s

on their suspended center on the trench (time-to-fracture *ca.* 10 s). We used either a diamond cono-spherical probe with a 25 μm tip radius, or a diamond spherical probe of 350 μm tip radius (depending on rod diameter).

The rods' Weibull coefficients were identified on the obtained force-displacement curves. For three-point bending, in the classical Euler framework, the failure probability according to Weibull theory writes:

$$P^F = 1 - \exp\left(-\frac{V}{V_0} H(m) \left(\frac{\bar{\sigma}}{\sigma_0}\right)^m\right) \quad (1)$$
$$\text{with} \quad \begin{cases} H(m) = \frac{\Gamma\left(\frac{m+1}{2}\right)}{2\sqrt{\pi}(m+2)\Gamma\left(\frac{m+2}{2}\right)} \\ \bar{\sigma} = Fl/\pi r^3 \end{cases}$$

where V is the rod's volume and V_0 a reference volume (in this paper we take $V_0 = 1\ mm^3$), $H(m)$ a stress heterogeneity factor involving the classical Γ function [Hild and Marquis, 1992], $\bar{\sigma}$ the Largest Positive Stress (LPS) in the rod, and σ_0 & m the two Weibull coefficients that have to be identified. This equation can be rewritten in the classical Weibull form:

$$\ln\left(\ln\left(\frac{1}{1-P^F}\right)\right) = m\ln(\bar{\sigma}) + \ln\left(\frac{V}{V_0}\right) + \ln(H(m)) - m\ln(\sigma_0) \quad (2)$$

Thus, for each rod (index i), one has:

$$\begin{cases} \bar{\sigma}_i^F = F_i^F l_i/\pi r_i^3 \\ V_i = \pi l_i r_i^2 \\ P_i^F = r/(N+1) \end{cases} \quad (3)$$

where N is the number of rods in the set, and r the rank of the rod i (the rod with the smallest LPS has $r = 1$; the one with the largest LPS has $r = N$). And for each set of rods, the Weibull coefficients were identified by computing the least-square plane that best fits the $\left(\bar{\sigma}_i^F, V_i, P_i^F\right)$ data in the $\left(\ln\left(\bar{\sigma}^F\right), \ln\left(\frac{V}{V_0}\right), \ln\left(\ln\left(\frac{1}{1-P^F}\right)\right)\right)$ space. Indeed, although the usual procedure computes the least-square line in the $\left(\ln\left(\bar{\sigma}^F\right), \ln\left(\ln\left(\frac{1}{1-P^F}\right)\right)\right)$ space, here the rods' diameter varies significantly, even in the same batch, and this must be taken into account in the identification process.

3. Modeling & Methods

3.1. Micro-Macro bridge

In this work, we use the Sanchez-Palencia theory of homogenization [Sanchez-Palencia, 1974], also called periodic or first-order asymptotic homogenization, to link the elastic behavior of the scaffolds and the one of their constitutive rods. Basically, this consists of *(i)* successively applying six macroscopic deformations $\underline{\underline{E}}^i$ (three extensions, three shears) on top of free periodic deformations to a cell ω representative of the microstructure (also called Representative Volume Element, RVE), *(ii)* computing the associated microscopic stress fields $\underline{\underline{\sigma}}^i$, and *(iii)* integrating them to obtain the corresponding macroscopic stress:

$$\underline{\underline{\Sigma}}^i = \frac{1}{|\omega|} \int_\omega \underline{\underline{\sigma}}^i \, d\omega \tag{4}$$

Finally, the homogenized stiffness tensor writes:

$$\widehat{\widehat{H}}_{ij} = \widehat{\Sigma}^i_j \tag{5}$$

(Engineering notations, denoted by $\widehat{\ }$, are used for simplicity.)

The underlying computations are performed using the finite element method (FEM). To take into account the scaffolds' complex microstructure (see Figure 1), level sets [Sethian, 1999] are used to represent the interfaces, and a selective integration method is used to handle variations of material properties [Moës et al., 2003; Genet, 2010]. Figure 2 presents a possible RVE. Each rod (index i) is located by *(i)* a point $\underline{X}_i$ of its middle line, *(ii)* the direction $\underline{N}_i$ of its middle line, and *(iii)* its diameter d_i. The associated level set function must *(i)* vanish at the rod's border, *(ii)* be positive inside the rod, and *(iii)* be negative outside. We take the following function:

$$\begin{aligned} \phi_i(\underline{x}) &= 1 - \frac{\|\underline{y} - {}^t\underline{N}_i \, \underline{y} \, \underline{N}_i\|}{d_i/2} \\ \text{with} \quad \underline{y} &= \underline{x} - \underline{X}_i \end{aligned} \tag{6}$$

Then a global level set function is built. It must be the Boolean sum of the level sets associated with all the rods in the RVE:

$$\phi(\underline{x}) = \max_i \left(\phi_i(\underline{x})\right) \tag{7}$$

Note that contrary to eXtended-FEM [Moës et al., 2003] and other methods with enhanced-kinematics elements [Jirasek, 2000; Benkemoun et al., 2010],

we do not introduce any discontinuity in the displacement or strain fields within the finite elements cut by the level set. Thus, the interfaces are somehow smoothed within the finite elements they cut, introducing another source of approximation within the FE solution. However, this method is particularly simple to implement, and is accurate enough for our needs [Moës et al., 2003; Genet, 2010]. (In all computations performed for this paper, we made sure the initial mesh was fine enough so the induced error on the homogenized stiffness was less than 1%. Typically, this entailed taking at least 10 elements per rod diameter.)

To perform FE computations, materials properties, *i.e.* Young modulus & Poisson ratio, must be prescribed for all integration points of the FE mesh, even those outside the rods. Also, they must be non-null in order to avoid having a singular stiffness matrix. We consider the following heterogeneous isotropic material properties:

$$\begin{cases} E\left(\underline{x}\right) = E^{\text{rod}} H\left(\phi\left(\underline{x}\right)\right) + \dfrac{E^{\text{rod}}}{M}\left(1 - H\left(\phi\left(\underline{x}\right)\right)\right) \\ \nu\left(\underline{x}\right) = \nu^{\text{rod}} H\left(\phi\left(\underline{x}\right)\right) \end{cases} \tag{8}$$

where E^{rod} & ν^{rod} are the rod's Young modulus & Poisson ratio, H the Heaviside function, and M a large number. (Typically, we took 10^6.) The stress fields are then post-treated using the following material properties:

$$\begin{cases} E\left(\underline{x}\right) = E^{\text{rod}} H\left(\phi\left(\underline{x}\right)\right) \\ \nu\left(\underline{x}\right) = \nu^{\text{rod}} H\left(\phi\left(\underline{x}\right)\right) \end{cases} \tag{9}$$

On a more technical basis, all meshes were generated using GMSH [Geuzaine and Remacle, 2009], and FE computations were done within the LMT++ library [Leclerc, 2010], which makes use of the CHOLMOD linear solver [Chen et al., 2008].

3.2. Macroscopic failure probability

After building the previous computational bridge between microscopic and macroscopic strain and stress fields, we use the Weibull theory of failure probability [Weibull, 1939, 1951] to predict the probability of failure of a given scaffold under a given load.

Basically, if the Weibull theory was first introduced based on phenomenological considerations [Weibull, 1939, 1951], it was later shown to rely on more fundamental basis: it is based on a Poisson process of the distribution of activated defects, the process intensity being a function of volume (with

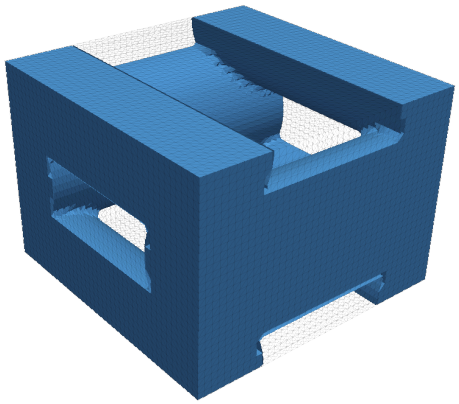

Figure 2: Computational periodic Representative Volume Element (RVE) of the robocast scaffolds used to link microscopic (*i.e.* rod) and macroscopic (*i.e.* scaffold) elastic properties through Sanchez-Palencia homogenization [Sanchez-Palencia, 1974]. The zero-level-set of the function representative of each single rod is visible, as are all elements fully inside each rod. The small distance between the elements and the surface is induced by use of a mesh that does not conform to the actual geometry.

linear dependence) and stress (with power dependence), and the weakest link principle [Freudenthal, 1968; Hild and Marquis, 1992]. In the case of a body of volume V submitted to an homogeneous uniaxial stress σ, the theory leads to the following widespread failure probability law:

$$P^F = 1 - \exp\left(-\frac{V}{V_0}\left(\frac{\sigma}{\sigma_0}\right)^m\right) \tag{10}$$

where σ_0 and m are the classical Weibull coefficients, and V_0 a reference volume. (Here we took $V_0 = 1\ mm^3$.)

Several extensions have been proposed to this law in order to take into account multiaxial stress fields [Evans, 1978; Lamon, 1988]. In this paper, we use a classical approach, based on the idea that only positive deformations will turn existing defects into propagating cracks, which has been experimentally evidenced for robocast scaffolds [Miranda et al., 2007], and used in several models *e.g.* for concrete [Desmorat, 2006] and ceramic matrix composites [Genet et al., 2012b]. Thus, we will consider the following probability law:

$$P^F = 1 - \exp\left(-\frac{1}{V_0}\int_V \left(\frac{\|\langle \underline{\underline{\epsilon}} \rangle_+\|}{\epsilon_0}\right)^m dV\right) \tag{11}$$

where $\langle \underline{\underline{\epsilon}} \rangle_+$ is the positive part of the deformation tensor, built by removing

all non-positive eigenvalues from $\underline{\underline{\epsilon}}$.

It is important to note that the integral of Equation (11) is theoretically defined over all the rods of the scaffold, *i.e.* on the whole microscopic domain, and is then non affordable *a priori*. However, thanks to the computational bridge built in Section 3.1, the computation of this integral can actually be split into two computations: one on the scaffold scale and one on the rod scale but on a single periodic cell. This splitting is illustrated in Figure 3. On the macroscopic scale, one has:

$$P^F = 1 - \exp\left(-\frac{1}{V_0}\int_\Omega I\left(\underline{\underline{E}}\left(\underline{X}\right)\right) d\Omega\right) \tag{12}$$

While for each macroscopic point, I is computed on the microscopic scale:

$$I\left(\underline{\underline{E}}\right) = \frac{1}{|\omega|}\int_\omega \left(\frac{\|\langle\underline{\underline{\epsilon}}^{\underline{\underline{E}}}\left(\underline{x}\right)\rangle_+\|}{\epsilon_0}\right)^m d\omega \tag{13}$$

Note that I is a non-linear function of $\underline{\underline{E}}$, and cannot be computed for a reduced set of basic deformations and then computed by linear combinations. As a consequence, it must actually be computed for every single macroscopic deformation.

In summary, the following steps are used to compute the failure probability of a given scaffold under a given load (see Figure 3):

- Thanks to the homogenized properties obtained in Section 3.1, the problem of the loaded scaffold is solved, and the macroscopic strain and stress fields are computed.
- For every required macroscopic point (typically, integration points), the microscopic strain and stress fields are computed, and the integral of Equation (13) is computed.
- Finally, the integral of Equation (12) is computed.

Thus, this strategy accounts for the influence of both structural parameters such as global volume and geometry (through the computation on the macroscopic scale, step 1) and microstructural parameters such a rod diameter and rod spacing (through the computation on the microscopic scale, step 2).

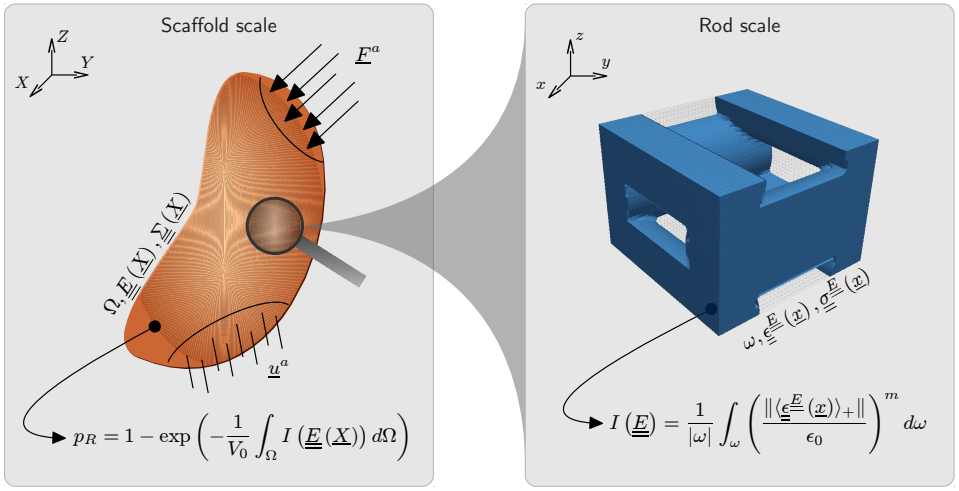

Figure 3: The proposed two-scale approach to predict the failure probability of a given scaffold under a given load. On the macroscopic scale (left), Ω denotes the volume of the scaffolds, and $\underline{\underline{E}}$ & $\underline{\underline{\Sigma}}$ the macroscopic strain and stress fields. On the microscopic scale (right), ω denotes the volume of the periodic representative cell, $\underline{\underline{\epsilon}}^{\underline{\underline{E}}}$ & $\underline{\underline{\sigma}}^{\underline{\underline{E}}}$ the microscopic strain and stress field associated with the macroscopic strain $\underline{\underline{E}}$, and ϵ_0 & m are the two Weibull coefficients.

3.3. Strength-Probability relations

For many materials, and especially ceramics, strength is not an actual intrinsic material parameters, as it is strongly probabilistic and most of all geometry- and load-dependent. Thus, the only intrinsic magnitudes are the parameters of the law giving strength distribution as a function of geometry and load, *i.e.* the Weibull-like law of Equation (12). However, another key magnitude is the strength associated with a given probability of failure of a given structure under a given load [Davidge et al., 1973; Gauthier and Lamon, 2009; Ladevèze and Genet, 2010], as it allows engineers to select materials and structures, and is the core of any certification process [Davidge et al., 1973]. It can be derived from the strength distribution as follows. For simplicity, consider that the macroscopic load is proportional to a scalar magnitude denoted σ (extension to more complex cases is straightforward):

$$\underline{F}^a\left(\underline{X}\right) = \sigma \underline{\bar{F}}^a\left(\underline{X}\right) \tag{14}$$

Thus, thanks to the linearity of the macroscopic problem, one has:

$$\underline{\underline{\Sigma}}\left(\underline{X}\right) = \sigma \underline{\underline{\bar{\Sigma}}}\left(\underline{X}\right), \quad \underline{\underline{E}}\left(\underline{X}\right) = \sigma \underline{\underline{\bar{E}}}\left(\underline{X}\right) \tag{15}$$

To express I as a simple function of σ, it is important to note the following property:

$$I\left(\sigma\underline{\underline{\bar{E}}}\right) = \sigma^m I\left(\underline{\underline{\bar{E}}}\right) \quad \forall\sigma > 0 \tag{16}$$

Thus, coupling Equations (12), (15) & (16), one obtains the structure strength σ^F associated with a given probability of failure P^F:

$$\sigma^F = \left(\frac{V_0}{\int_\Omega I\left(\underline{\underline{\bar{E}}}\left(\underline{X}\right)\right) d\Omega} \ln\left(\frac{1}{1-P^F}\right)\right)^{1/m} \tag{17}$$

4. Results & Discussion

4.1. Experimental results

4.1.1. Uniaxial compression of scaffolds

Two representative force-displacement curves are presented in Figure 4. They both present a first stage with successive failures of non-critical rods (that do not cause the failure of the scaffold as a whole), and then, after the failure of the critical rod, a second stage of relatively sharp failure of the whole scaffold. This indicates that the scaffold's failure in compression is not brittle, but quasi-brittle: it requires multiple lines breaking before final failure.

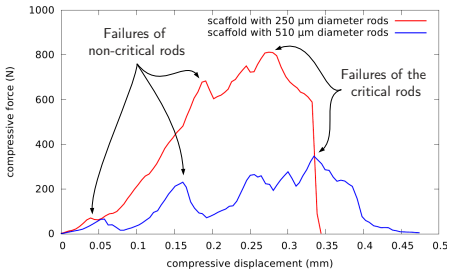

Figure 4: Representative force-displacement curves of the uniaxial (vertical) compression tests performed on robocast scaffolds. Shown are two examples of scaffolds printed respectively with a 250 μm-diameter tip and a 490 μm-spacing between the lines (both before sintering), and with a 510 μm-diameter tip and a 830 μm-spacing between the lines (both before sintering).

Figure 5 presents the compressive strength for each set of scaffolds. Strength varies significantly from one morphology to another even when

changing both rods spacing and diameter so as to keep the porosity constant (see Figure 5(a)). The porosity-dependence of strength for a given rod diameter (250 μm before sintering) is presented in Figure 5(b).

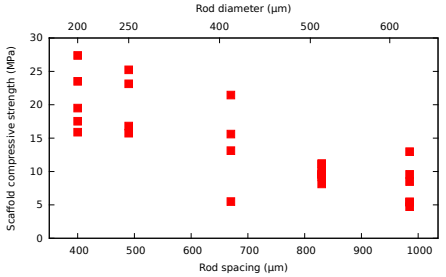

(a) Batch $S^{\mathrm{HA}}_{V=45\%}$, *i.e.* HA scaffolds with constant porosity (45%)

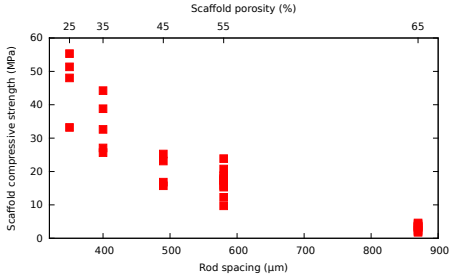

(b) Batch $S^{\mathrm{HA}}_{d=250\mu m}$, *i.e.* HA scaffolds with constant rod diameter (250 μm before sintering)

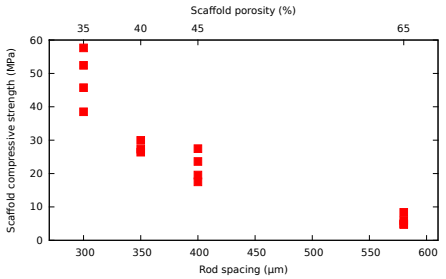

(c) Batch $S^{\mathrm{HA}}_{d=200\mu m}$, *i.e.* HA scaffolds with constant rod diameter (200 μm before sintering)

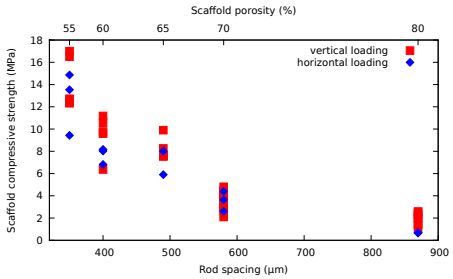

(d) Batch $S^{\mathrm{HA/TCP}}_{d=250\mu m}$, *i.e.* HA/TCP scaffolds with constant rod diameter (250 μm before sintering)

Figure 5: Compressive strength of scaffolds with multiple rods diameter and center-to-center spacing (every point corresponds to an individual test). One can see in (a) that even for scaffolds with constant porosity, strength depends on the rods diameter and spacing; and in (b), (c) & (d) the porosity-dependence of strength for multiple materials, rod diameters and loading directions.

4.1.2. Three-point bending of single rods

The force-displacement curves (not represented) present a linear regime, followed by a sharp failure, indicating that the rod's failure in bending is fully brittle.

Table 1 presents the average strength measured for each batch of rods, as well as the standard deviation of each distribution. The printing process uses inks with relatively high water and organic components, resulting in

a significant amount of microporosity within the rods [Franco et al., 2010; Houmard et al., 2012a]. These micropores are defects from the mechanical point of view, which explains the variability in the data. It is important to note that for some biological applications, microporosity is required so a balance must be found between biological and mechanical properties. The strong volume-dependence and high scattering in the data illustrate the need for a robust statistical analysis based on the Weibull theory.

Batch	Average Strength (MPa)	Standard deviation (MPa)
$R_{d=250\mu m}$	190	109
$R_{d=510\mu m}$	119	34
$R_{d=840\mu m}$	110	36

Table 1: Average strength and standard deviation for each set of rods. On top of the orders of magnitude, one can see here the important volume-dependence and scattering of the rods' strength, establishing the need for a Weibull analysis.

Figure 6 presents the computed values of Weibull coefficients for each set of rods. It was checked that these values are statistically converged. Both σ_0 and m are found to depend on rod diameter, the dependence being linear. As a consequence, the rods' Weibull coefficients are not intrinsic, *i.e.* the distribution of defects depends on rod diameter. This is probably induced by the problems associated with drying and the burn out of the ink's organic components in larger rods, as well as the variations in local sintering conditions for rods with different diameters (even though the global sintering conditions are similar for all single rods), which has been shown to modify the average shape of pores for hydroxylapatite [Prokopiev and Sevostianov, 2006]. Moreover, solvent elimination/drying could be different for different rod diameters, resulting in different pores populations.

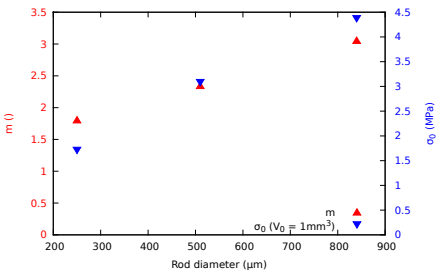

Figure 6: Weibull coefficients of single rods as a function of their diameter. One can see the linear dependence of the coefficients to the rod diameter.

4.1.3. Summary & Discussion

If the porosity-dependence of the scaffold's compressive strength illustrated on Figures 5(b), 5(c) & 5(d) is a rather expected tendency, the architecture-dependence illustrated on Figure 5(a) needs to be further discussed. Indeed, two mechanisms can be responsible for this: *(i)* the variations in rods' failure properties with regard to their diameter; and *(ii)* the variations in the sequence of rods failure from the onset of damage to final failure, with regard to rods diameter. Thus, it is necessary to investigate all potential scenarios to establish the importance of each in the failure of robocast scaffolds. Such an investigation has been carried out based upon the computational modeling described in Section 3, and its outcome is presented below.

4.2. Strength predictions

Here we apply the strength modeling framework described in Section 3.3 to the experimental conditions of Sections 2.1, *i.e.* cubic scaffolds under uniaxial compression (the compressive stress is denoted σ). Thus, the mechanical problem can be solved analytically, and leads to simple homogeneous macroscopic fields:

$$\underline{\underline{\Sigma}} = \begin{pmatrix} 0 & 0 & 0 \\ 0 & 0 & 0 \\ 0 & 0 & -\sigma \end{pmatrix}, \quad \underline{\underline{E}} = \begin{pmatrix} \dfrac{\widetilde{\nu}_{13}\sigma}{\widetilde{E}_1} & 0 & 0 \\ 0 & \dfrac{\widetilde{\nu}_{12}\sigma}{\widetilde{E}_1} & 0 \\ 0 & 0 & \dfrac{-\sigma}{\widetilde{E}_3} \end{pmatrix} \tag{18}$$

where the $\widetilde{\ }$ variables are the homogenized Young moduli & Poisson ratios of the scaffolds. Having an homogeneous solution of the macroscopic problem greatly simplifies the computation of Equations (12) & (13).

For the rods elastic properties, we used the ones measured through microindentation in [Miranda et al., 2008b]. They are presented in Table 2. Elastic properties of HA/TCP rods were interpolated between pure HA and pure TCP rods properties through the rule of mixture.

	HA	TCP
Young modulus (GPa)	82	36
Poisson ratio ()	0.28	0.28

Table 2: Elastic properties of HA & TCP rods, as reported in [Miranda et al., 2008b].

The model predictions for the scaffolds' strength relies on two scalar parameters: the rods' Weibull coefficients ϵ_0 & m, which characterize a population of defects (see Section 3.2). The experimental data used to identify these parameters determine the considered population of defects, and then the outcome of the model. Two sets of data are considered here: *(i)* the one on the rod scale (see Section 4.1.2), thus following a *bottom-up* approach, and *(ii)* the one on the scaffold scale (see Section 4.1.1), thus following a *top-down* approach.

4.2.1. Predictions based on rod data

When considering data on the rod scale (see Section 4.1.2, especially Figure 6, with $\epsilon_0 = \sigma_0/E^{\text{rod}}$) to predict the failure of a whole scaffold through the two-scale Weibull model proposed here, one actually considers that the failure of a single rod in the scaffold leads to the failure of the whole scaffold. It is an extremely conservative hypothesis, but it is used in several models in the literature, especially models for brittle materials with industrial applications [Cluzel et al., 2009; Genet et al., 2012a].

However, in our case, such an hypothesis is far too conservative, and scaffolds out-of-plane strength predictions (not shown) are much lower ($< 10\%$) than experimental values. Furthermore, the model does not reproduce the morphological dependence of the strength, either for scaffolds with constant porosity or for scaffolds with constant rod diameter. This establishes that even if variations in rods' Weibull moduli with regard to rod diameter have a slight role in scaffold strength, it is not the main mechanism in scaffold failure. As a consequence, the successive breaking of rods must be the key mechanism to the scaffold's final failure, and must be rod diameter-dependent: for scaffolds with small rods diameter, the stress level can be drastically increased even after several single rods break; this is not the case for scaffolds with large rods diameter.

4.2.2. Predictions based on scaffold data

When considering the data on the scaffold scale (see Section 4.1.1) to predict the failure of scaffolds through the two-scale Weibull model proposed here, one does not consider anymore the largest microdefects present within the scaffolds (which are responsible for the failure of the first single rods), but the critical ones, *i.e.* the ones responsible for the failure of the whole scaffold (see Figure 4). In other words, the model tracks the failure of the critical rod, *i.e.* the one that finally causes the whole scaffold to fail. And as the successive failures of rods toward the scaffolds' final failure is a rod

diameter-dependent phenomenon, a set of Weibull coefficients characterizing the scaffolds critical defects must be identified for each rod diameter.

HA scaffolds. For HA scaffolds, the batch $S^{\mathrm{HA}}_{V=45\%}$ was used as it contains scaffolds with same porosity but multiple rod diameter. Figure 7 & Table 3 present the outcome of this identification process, made through the best-fit method. For the sake of simplicity, we have kept the dispersion coefficient m equal for all scaffolds, while changing only the mean coefficient σ_0. The fact that σ_0 decreases very significantly with rod diameter is related to the fact that breaking a single rod of small diameter is less critical than breaking a single rod of large diameter, even in scaffolds with the same overall porosity.

Figure 8 presents the scaffolds' out-of-plane strength predicted by the proposed model based upon this identification, compared with the experimentally measured ones (see Section 4.1.1): one can clearly see that it is suitable to predict the strength of scaffolds with a large range of rods spacing, *i.e.* of scaffold porosity, outside the identification domain. In other words, based on the data of a single set of scaffolds with one line diameter and one macroporosity, the proposed two-scale Weibull model can predict the behavior of scaffolds with a wide range or macroporosities. As a consequence, using numerical optimization [Allaire et al., 2002], it could be used to find optimal scaffold design (with optimal shape and optimal graded porosity) with regard to strength for a given application (*i.e.* given fixations, given load). The only restriction regarding strength optimization is to keep the rod diameter constant, which is imposed by the process anyway.

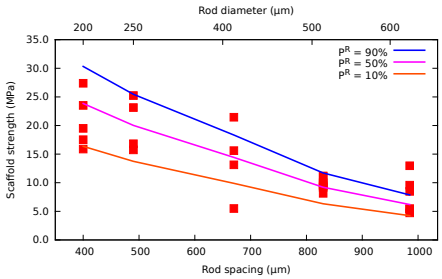

Figure 7: Identification of the HA rods' Weibull coefficients characterizing the population of HA scaffold critical defects based on scaffold scale data. Batch $S^{\mathrm{HA}}_{V=45\%}$ is used so as to identify a set of Weibull coefficients for each rod diameter.

HA/TCP scaffolds. For HA/TCP scaffolds, scaffolds with only one rod diameter (250 μm) were printed. One particular printing configuration (rod spacing 590 μm, porosity 70 %) and loading condition (vertical compression)

d (μm)	200	250	410	510	610
m $()$	5	5	5	5	5
σ_0 (MPa)	180	140	70	45	30

Table 3: HA rods' Weibull coefficients characterizing the population of critical defects in HA scaffolds, *i.e.* the ones responsible for the scaffolds' final failure. The large diameter-dependence of these coefficients, despite the fact that rods' Weibull coefficients characterizing their largest defects (*i.e.* the one responsible for the failure of the first rod) are only slightly diameter-dependent, is induced by the rod diameter-dependence of the successive failures of rods in the scaffold. This phenomenon is not explicitly modeled in the proposed approach, but implicitly through this diameter-dependence of the Weibull coefficients.

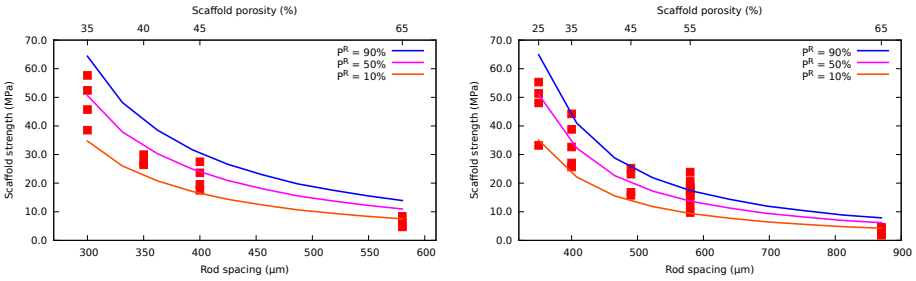

(a) Batch $S^{\mathrm{HA}}_{d=200\mu m}$, *i.e.* HA scaffolds with constant rods diameter (200 μm before sintering)

(b) Batch $S^{\mathrm{HA}}_{d=250\mu m}$, *i.e.* HA scaffolds with constant rods diameter (250 μm before sintering)

Figure 8: Comparison of the HA scaffolds' out-of-plane strength predicted through the proposed two-scale Weibull model and measured experimentally. It can be seen that for a given diameter, the model can predict scaffold strength for a large range of porosities, outside the calibration domain.

was used to calibrate the model's parameters. Table 4 presents the outcome of this identification process, once again made through the best-fit method. Figure 9 presents the scaffolds' out-of-plane and in-plane strength predicted by the proposed model based upon this identification, compared with the experimentally measured ones (see Section 4.1.1). Once again the model is shown to suitably predict the strength of scaffolds with a large range of rods spacing, *i.e.* of scaffold porosity. Moreover, it is shown to provide satisfying predictions for different loading condition with regard to the calibration loading condition.

m $()$	σ_0 (MPa)
5	38

Table 4: HA/TCP rods' Weibull coefficients characterizing the population of critical defects in the scaffolds.

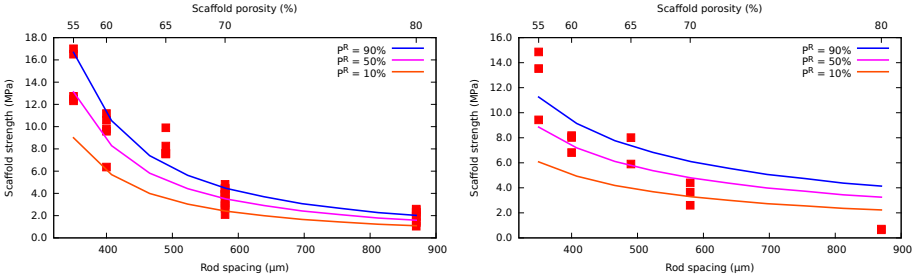

(a) Batch $S^{\mathrm{HA/TCP}}_{d=250\mu m}$, *i.e.* HA/TCP scaffolds with constant rods diameter (250 μm before sintering), loaded vertically

(b) Batch $S^{\mathrm{HA/TCP}}_{d=250\mu m}$, *i.e.* HA/TCP scaffolds with constant rods diameter (250 μm before sintering), loaded horizontally

Figure 9: Comparison of the HA/TCP scaffolds' out-of-plane strength predicted through the proposed two-scale Weibull model and measured experimentally. It can be seen that the model can predict scaffold strength for a large range of porosities and several loading conditions, outside the calibration domain.

5. Conclusion

In this paper, we have introduced a new two-scale model of the mechanics of hierarchical quasi-brittle materials, by the example of calcium phosphate scaffolds made by robocasting for bone-tissue engineering applications. The domain of validity and the different possibilities offered by this model have been studied based on two sets of experimental data: uniaxial compression

tests on scaffolds and three-point bending tests on single rods. While the former has been detailed in [Houmard et al., 2012a], the latter is presented here for the first time, and leads to an interesting fact: rods' Weibull coefficients are actually rod diameter-dependent, meaning that the population of defects is different in rods printed with different tip diameters.

At the core of the proposed model, the rod and scaffold scales are linked through the Sanchez-Palencia's theory of periodic homogenization [Sanchez-Palencia, 1974]. Furthermore, scaffold strength is predicted through the Weibull's theory of failure probability [Weibull, 1939, 1951]. The Weibull integral is computed on the rod scale, and transferred at the scaffold scale thanks to the computational bridge established between microscopic and macroscopic strain and stress fields. This allows to account for both microstructural and structural effects, and then to study with a single model the influence of *e.g.* rod diameter, rod spacing, scaffold size, *etc.*

The model has been calibrated in two ways: directly from the rod scale experimental data (*i.e.* following a bottom-up approach) and by fitting the scaffold scale experimental data (*i.e.* following a top-down approach). Both ways lead to very different answers, meaning that two different populations of defects have been identified. When calibrating the rods' Weibull coefficients based on the rods three-point bending tests, one actually characterizes the population of rods' largest defects. Transferred to the scaffold scale, this leads to very conservative predictions that are not compatible with experimental data, as it is necessary to take into account the successive failures of rods within the scaffolds from the onset of damage to the final failure. This process can be implicitly handled in the proposed model by calibrating the rods' Weibull coefficients from the uniaxial compression tests on scaffolds, which means that one actually characterizes the population of critical defects, *i.e.* those responsible for the scaffold's final failure. This allowed us to make the model compatible with all available experimental data on the scaffold's scale.

It is important to point out that if the rods Weibull modulus was very high, then the failure of a single rod would trigger the failure of all other rods, and would induce the failure of the scaffold, and modeling the link between rod and scaffold failure would be more straightforward. However, in the more realistic case investigated here where rods Weibull modulus are pretty low, multiple single rod failures, all at different stress levels, are necessary to break the scaffolds, and the modeling becomes more involved. Thus, the present model appears to be a good compromise between modeling effort and prediction capabilities. Indeed, even though numerical simulation is required on the rod scale, and experimental calibration from scaffold scale data is

required for each rod diameter, the model has been shown to accurately predict the strength distributions of a wide range of scaffolds, with given rod diameter but varying porosities, far away from the calibration domain, and under loading conditions different from the calibration ones.

Consequently, the present model could be used to find optimal printing patterns, with regard to stiffness and strength, for specific geometries and mechanical loads. Indeed, novel scaffold designs are now being investigated for application in multiple domains such as tissue engineering. For instance, there were attempts to mimic the structure of real bone, with low porosity at the scaffold's surface, and higher porosity toward its core. (Other example are presented in [Houmard et al., 2012a].) Thus, with graded porosity, the scaffold design domains become too vast to be explored without the help and guidance from a computational model such as the one introduced in this paper. Numerical optimization (see for instance [Allaire et al., 2002]) will have to be used, based on multiscale models as the one presented here, in order to process truly optimal scaffold for each application.

Acknowledgment

This work was supported by the National Institutes of Health/National Institute of Dental and Craniofacial Research (NIH/NIDCR) Grant No. 1R01DE015633. The authors would also like to thank Ms. Grace Lau for her help in robocast scaffolds and single rods processing.

References

Grégoire Allaire, François Jouve, and Anca-Maria Toader. A level-set method for shape optimization. *Comptes Rendus à l'Académie des Sciences, Série I*, 334:1125–1130, 2002.

Nathan Benkemoun, Martin Hautefeuille, Jean-Baptiste Colliat, and Adnan Ibrahimbegovic. Failure of heterogeneous materials: 3D meso-scale FE models with embedded discontinuities. *International Journal for Numerical Methods in Engineering*, 82(13):1671–1688, 2010. ISSN 00295981. DOI 10.1002/nme.2816.

Yanqing Chen, Timothy A. Davis, William W. Hager, and Sivasankaran Rajamanickam. Algorithm 887: CHOLMOD, supernodal sparse Cholesky factorization and update/downdate. *ACM Transactions on Mathematical Software*, 35(3):1–14, October 2008. ISSN 00983500. DOI 10.1145/1391989.1391995.

Christophe Cluzel, Emmanuel Baranger, Pierre Ladevèze, and Anne Mouret. Mechanical behaviour and lifetime modelling of self-healing ceramic-matrix composites subjected to thermomechanical loading in air. *Composites Part A: Applied Science and Manufacturing*, 40(8):976–984, August 2009. ISSN 1359835X. DOI 10.1016/j.compositesa.2008.10.020.

R. W. Davidge, J. R. McLaren, and G. Tappin. Strength-Probability-Time (SPT) relationships in ceramics. *Journal of Materials Science*, 8(12): 1699–1705, December 1973. ISSN 0022-2461. DOI 10.1007/BF02403519.

Rodrigue Desmorat. Positivity of intrinsic dissipation of a class of nonstandard anisotropic damage models. *Comptes Rendus Mécanique*, 334(10): 587–592, October 2006. DOI 10.1016/j.crme.2006.07.015.

Anthony G. Evans. A General Approach for the Statistical Analysis of Multiaxial Fracture. *Journal of the American Ceramic Society*, 61(7-8):302–308, July 1978. ISSN 0002-7820. DOI 10.1111/j.1151-2916.1978.tb09314.x.

Jaime Franco, Philipp M. Hunger, Maximilien E. Launey, Antoni P. Tomsia, and Eduardo Saiz. Direct write assembly of calcium phosphate scaffolds using a water-based hydrogel. *Acta Biomaterialia*, 6(1):218–28, January 2010. ISSN 1878-7568. DOI 10.1016/j.actbio.2009.06.031.

A. M. Freudenthal. Statistical approach to brittle fracture. In H. Liebowitz, editor, *Fracture*, pages 591–619. Academic Press, 1968.

Qiang Fu, Eduardo Saiz, Mohamed N. Rahaman, and Antoni P. Tomsia. Bioactive glass scaffolds for bone tissue engineering: state of the art and future perspectives. *Materials science & engineering. C, Materials for biological applications*, 31(7):1245–1256, October 2011. ISSN 0928-4931. DOI 10.1016/j.msec.2011.04.022.

Wilfried Gauthier and Jacques Lamon. Delayed Failure of Hi-Nicalon and Hi-Nicalon S Multifilament Tows and Single Filaments at Intermediate Temperatures (500°-800°C). *Journal of the American Ceramic Society*, 92(3):702–709, March 2009. ISSN 00027820. DOI 10.1111/j.1551-2916.2009.02924.x. URL `http://doi.wiley.com/10.1111/j.1551-2916.2009.02924.x`.

Martin Genet. *Toward a virtual material for ceramic composites (in French)*. Phd thesis, ENS-Cachan, 2010.

Martin Genet, Lionel Marcin, Emmanuel Baranger, Christophe Cluzel, Pierre Ladevèze, and Anne Mouret. Computational prediction of the lifetime of self-healing CMC structures. *Composites Part A: Applied Science and Manufacturing*, 43(2):294–303, February 2012a. ISSN 1359835X. DOI 10.1016/j.compositesa.2011.11.004.

Martin Genet, Lionel Marcin, and Pierre Ladevèze. On structural computations until fracture based on an anisotropic and unilateral damage theory. *Submitted to the International Journal of Damage Mechanics (In Third Review)*, 2012b.

Christophe Geuzaine and Jean-François Remacle. Gmsh: a three-dimensional finite element mesh generator with built-in pre- and post-processing facilities. *International Journal for Numerical Methods in Engineering*, 79(11):1309–1331, September 2009. ISSN 00295981. DOI 10.1002/nme.2579.

Gregory M. Gratson, Florencio García-Santamaría, Virginie Lousse, Mingjie Xu, Shanhui Fan, Jennifer A. Lewis, and Paul V. Braun. Direct-Write Assembly of Three-Dimensional Photonic Crystals: Conversion of Polymer Scaffolds to Silicon Hollow-Woodpile Structures. *Advanced Materials*, 18(4):461–465, February 2006. ISSN 0935-9648. DOI 10.1002/adma.200501447.

François Hild and Didier Marquis. A statistical approach to the rupture of brittle materials. *European Journal of Mechanics Part A: Solids*, 11(6): 753–765, 1992. ISSN 0997-7538.

Manuel Houmard, Qiang Fu, Martin Genet, Eduardo Saiz, and Antoni P. Tomsia. Effect of the HA/β-TCP composition on the properties of robocast calcium phosphate scaffolds. *Submitted to the Journal of Materials Science: Materials in Medicine*, 2012a.

Manuel Houmard, Qiang Fu, Eduardo Saiz, and Antoni P. Tomsia. Sol-gel method to fabricate CaP scaffolds by robocasting for tissue engineering. *Journal of Materials Science: Materials in Medicine*, 23(4):921–30, April 2012b. ISSN 1573-4838. DOI 10.1007/s10856-012-4561-2.

Milan Jirasek. Comparative study on finite elements with embedded discontinuities. *Computer Methods in Applied Mechanics and Engineering*, 188(1-3):307–330, July 2000. ISSN 00457825. DOI 10.1016/S0045-7825(99)00154-1.

Pierre Ladevèze and Martin Genet. A new approach to the subcritical cracking of ceramic fibers. *Composites Science and Technology*, 70(11):1575–1583, October 2010. ISSN 02663538. DOI 10.1016/j.compscitech.2010.04.013.

Jacques Lamon. Statistical Approaches to Failure for Ceramic Reliability Assessment. *Journal of the American Ceramic Society*, 71(2):106–112, January 1988. DOI 10.1016/S0267-7261(88)80013-7.

Sheeny K. Lan Levengood, Samentha J. Polak, Matthew B. Wheeler, Aaron J. Maki, Sherrie G. Clark, Russell D. Jamison, and Amy J. Wagoner Johnson. Multiscale osteointegration as a new paradigm for the design of calcium phosphate scaffolds for bone regeneration. *Biomaterials*, 31(13):3552–63, May 2010. ISSN 1878-5905. DOI 10.1016/j.biomaterials.2010.01.052.

Hugo Leclerc. Towards a no compromise approach between modularity, versatility and execution speed for computational mechanics on CPUs and GPUs. In *IV European Conference on Computational Mechanics (ECCM2010)*, 2010.

K.F. Leong, C.M. Cheah, and C.K. Chua. Solid freeform fabrication of three-dimensional scaffolds for engineering replacement tissues and organs. *Biomaterials*, 24(13):2363–2378, June 2003. ISSN 01429612. DOI 10.1016/S0142-9612(03)00030-9.

Xiaoxing Liu, Christrophe L. Martin, Didier Bouvard, Stephane Di Iorio, Jérôme Laurencin, and Gérard Delette. Strength of Highly Porous Ceramic Electrodes. *Journal of the American Ceramic Society*, 94(10):3500–3508, 2011. DOI 10.1111/j.1551-2916.2011.04669.x.

L. McIntosh, J. M. Cordell, and Amy J. Wagoner Johnson. Impact of bone geometry on effective properties of bone scaffolds. *Acta Biomaterialia*, 5(2):680–92, March 2009. ISSN 1878-7568. DOI 10.1016/j.actbio.2008.09.010.

Pedro Miranda, Eduardo Saiz, Karol Gryn, and Antoni P. Tomsia. Sintering and robocasting of beta-tricalcium phosphate scaffolds for orthopaedic applications. *Acta biomaterialia*, 2(4):457–66, July 2006. ISSN 1742-7061. DOI 10.1016/j.actbio.2006.02.004.

Pedro Miranda, Antonia Pajares, Eduardo Saiz, Antoni P. Tomsia, and Fernando Guiberteau. Fracture modes under uniaxial compression in hydroxyapatite scaffolds fabricated by robocasting. *Journal of biomedical materials research. Part A*, 83(3):646–55, December 2007. ISSN 1549-3296. DOI 10.1002/jbm.a.31272.

Pedro Miranda, Antonia Pajares, and Fernando Guiberteau. Finite element modeling as a tool for predicting the fracture behavior of robocast scaffolds. *Acta biomaterialia*, 4(6):1715–24, November 2008a. ISSN 1878-7568. DOI 10.1016/j.actbio.2008.05.020.

Pedro Miranda, Antonia Pajares, Eduardo Saiz, Antoni P. Tomsia, and Fernando Guiberteau. Mechanical properties of calcium phosphate scaffolds fabricated by robocasting. *Journal of biomedical materials research. Part A*, 85(1):218–27, April 2008b. ISSN 1552-4965. DOI 10.1002/jbm.a.31587.

Nicolas Moës, Mathieu Cloirec, P. Cartraud, and Jean-François Remacle. A computational approach to handle complex microstructure geometries. *Computer Methods in Applied Mechanics and Engineering*, 192 (28-30):3163–3177, July 2003. ISSN 00457825. DOI 10.1016/S0045-7825(03)00346-3.

Oleg Prokopiev and Igor Sevostianov. Dependence of the mechanical properties of sintered hydroxyapatite on the sintering temperature. *Materials Science and Engineering: A*, 431(1-2):218–227, September 2006. ISSN 09215093. DOI 10.1016/j.msea.2006.05.158.

J. Russias, Eduardo Saiz, Sylvain Deville, Karol Gryn, G. Liu, R. K. Nalla, and Antoni P. Tomsia. Fabrication and in vitro characterization of three-dimensional organic/inorganic scaffolds by robocasting. *Journal of Biomedical Materials Research Part A*, 83(2):434–45, November 2007. ISSN 1549-3296. DOI 10.1002/jbm.a.31237.

Eduardo Saiz, Laurent Gremillard, G. Menendez, Pedro Miranda, Karol Gryn, and Antoni P. Tomsia. Preparation of porous hydroxyapatite scaffolds. *Materials Science and Engineering: C*, 27(3):546–550, April 2007. ISSN 09284931. DOI 10.1016/j.msec.2006.05.038.

Enrique Sanchez-Palencia. Comportements local et macroscopique d'un type de milieux physiques hétérogènes. *International Journal of Engineering Science*, 12(4):331–351, April 1974. ISSN 00207225. DOI 10.1016/0020-7225(74)90062-7.

James A. Sethian. *Level Set Methods and Fast Marching Methods: Evolving Interfaces in Computational Geometry, Fluid Mechanics, Computer Vision, and Materials Science—Second Edition.* Cambridge University Press—Cambridge Monographs on Applied and Computational Mathematics, 1999. ISBN 9780521645577. DOI 10.2277/0521645573.

James E. Smay, Joseph Cesarano III, and Jennifer A. Lewis. Colloidal Inks for Directed Assembly of 3-D Periodic Structures. *Langmuir*, 84(18):5429–5437, 2002.

Wallodi Weibull. A statistical theory of the strength of materials. *Royal Swedish Institute for Engineering Research*, 151, 1939.

Wallodi Weibull. A statistical distribution function of wide applicability. *Journal of Applied Mechanics*, pages 293–297, September 1951.

Joseph R. Woodard, Amanda J. Hilldore, Sheeny K. Lan, C. J. Park, Abby W. Morgan, Jo Ann C. Eurell, Sherrie G. Clark, Matthew B. Wheeler, Russell D. Jamison, and Amy J. Wagoner Johnson. The mechanical properties and osteoconductivity of hydroxyapatite bone scaffolds with multi-scale porosity. *Biomaterials*, 28(1):45–54, January 2007. ISSN 0142-9612. DOI 10.1016/j.biomaterials.2006.08.021.

H. Y. Yang, X. P. Chi, S. Yang, and Julian R. G. Evans. Mechanical strength of extrusion freeformed calcium phosphate filaments. *Journal of Materials Science: Materials in Medicine*, 21(5):1503–1510, May 2010. ISSN 1573-4838. DOI 10.1007/s10856-010-4009-5.